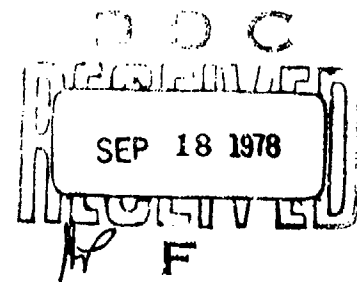**LEVEL**

RADC-TR-76-382
Technical Report
December 1976

PRECOMPENSATION AND POSTCOMPENSATION OF PHOTON
LIMITED DEGRADED IMAGES

Stanford University

Sponsored By
Defense Advanced Research Projects Agency (DoD)
ARPA Order No. 2646

Approved for public release;
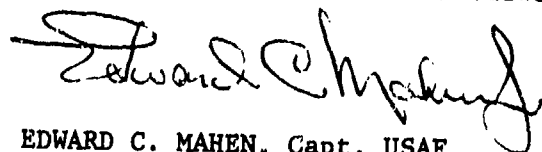distribution unlimited.

DDC

SEP 18 1978

F

The views and conclusions contained in this document are those of the
authors and should not be interpreted as necessarily representing the
official policies, either expressed or implied, of the Defense
Advanced Research Projects Agency or the U. S. Government.

ROME AIR DEVELOPMENT CENTER
AIR FORCE SYSTEMS COMMAND
FFISS AIR FORCE BASE, NEW YORK 1344

78 09 11 082

This report has been reviewed by the RADC Information Office (OI) and is releasable to the National Technical Information Service (NTIS). At NTIS it will be releasable to the general public including foreign nations.

This report has been reviewed and is approved for publication.

EDWARD C. MAHEN, Capt, USAF
Project Engineer

Do not return this copy. Retain or destroy.

PRECOMPENSATION AND POSTCOMPENSATION OF PHOTON
LIMITED DEGRADED IMAGES

J. W. Goodman
J. F. Belsher

Approved for public release;
distribution unlimited.

REPORT DOCUMENTATION PAGE

READ INSTRUCTIONS
BEFORE COMPLETING FORM

1. REPORT NUMBER	2. GOVT ACCESSION NO.	3. RECIPIENT'S CATALOG NUMBER
RADC-TR-76-382		

4. TITLE *(and Subtitle)*	5. TYPE OF REPORT & PERIOD COVERED
PRECOMPENSATION AND POSTCOMPENSATION OF PHOTON LIMITED DEGRADED IMAGES	Interim Report 1 Feb 75 - 30 Jun 76
	6. PERFORMING ORG. REPORT NUMBER N/A

7. AUTHOR(s)	8. CONTRACT OR GRANT NUMBER(s)
J. W. Goodman J. F. Belsher	F30602-75-C-0228 ARPA Order-2646

9. PERFORMING ORGANIZATION NAME AND ADDRESS	10. PROGRAM ELEMENT, PROJECT, TASK AREA & WORK UNIT NUMBERS
Stanford University Stanford CA 94305	62301E 26460405

11. CONTROLLING OFFICE NAME AND ADDRESS	12. REPORT DATE
Defense Advanced Research Projects Agency 1400 Wilson Blvd Arlington VA 22209	December 1976
	13. NUMBER OF PAGES 25

14. MONITORING AGENCY NAME & ADDRESS *(if different from Controlling Office)*	15. SECURITY CLASS. *(of this report)*
Rome Air Development Center (OCSE) Griffiss AFB NY 13441	UNCLASSIFIED
	15a. DECLASSIFICATION/DOWNGRADING SCHEDULE N/A

16. DISTRIBUTION STATEMENT *(of this Report)*

Approved for public release; distribution unlimited.

17. DISTRIBUTION STATEMENT *(of the abstract entered in Block 20, if different from Report)*

Same

18. SUPPLEMENTARY NOTES

RADC Project Engineer:
Capt. Edward C. Mahen (OCSE)

19. KEY WORDS *(Continue on reverse side if necessary and identify by block number)*

Speckle Imaging
Image Processing
Coherent Optics

20. ABSTRACT *(Continue on reverse side if necessary and identify by block number)*

New results are presented on the problem of linear least-squares restoration of photon-limited, atmospherically degraded images.

The photon-limited performance of a system which combines pre-detection compensation and post-detection compensation is considered.

We present some recently obtained results on the photon-limited sensitivity

CONT'

DD FORM 1473 EDITION OF 1 NOV 65 IS OBSOLETE
1 JAN 73

CONT

of the "speckle imaging" technique for obtaining high resolution object information in the presence of atmospheric turbulence.

I.   INTRODUCTION

This report addresses three problems. First, new results are
presented on the problem of linear least-squares restoration of photon-
limited, atmospherically degraded images. Second, the photon-limited
performance of a system which combines pre-detection compensation and
post-detection compensation is considered. Thirdly, we present some
recently obtained results on the photon-limited sensitivity of the
"speckle imaging" technique for obtaining high resolution object inform-
ation in the presence of atmospheric turbulence.

The analysis and results presented in this report depend heavily
on material published in a previous technical report [1]. As far as
possible, the notation in this report is identical to that used in the
former, except for a few small improvements. We shall feel free to call
upon the previously derived results as needed.

II.   BACKGROUND

The problem addressed here is illustrated in Fig 1. A distant
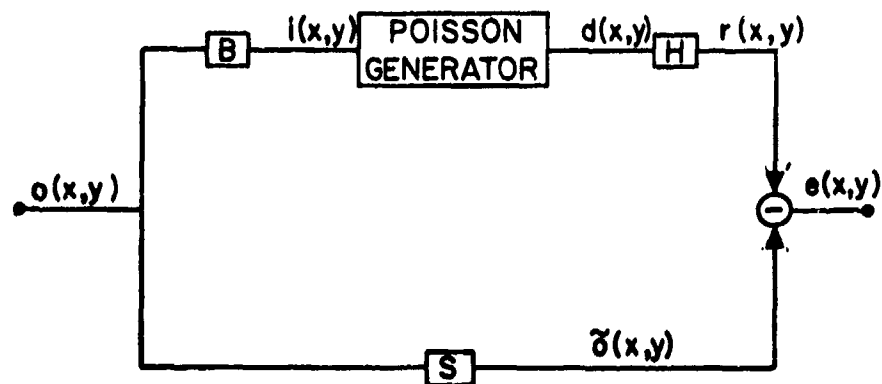object, represented by a radiance distribution $o(x,y)$, is subjected to

Fig. 1. Block diagram for least-mean-square-error restoration

- 1 -

a linear, isoplanatic blur, represented by optical transfer function $\hat{B}(\Omega_X, \Omega_Y)$. (The spatial frequencies Ω_X and Ω_Y are measured in cycles per radian of arc in the sky.) In the case of special interest here, this blur arises from both atmospheric inhomogeneities and diffraction due to the finite aperture of the telescope used. The blurred irradiance distribution $i(x,y)$ is then detected. The detected signal $d(x,y)$ is represented as a compound Poisson process, with space variant mean $\lambda(x,y)$ proportional to $i(x,y)$. The detected signal is passed through a linear space-invariant restoration filter with transfer function $H(\Omega_X, \Omega_Y)$.

The restoration filter is chosen to minimize the mean-squared value of the error $e(x,y)$, which represents the difference between the restored image $r(x,y)$ and an "ideally" filtered version of the object $\tilde{o}(x,y)$. The ideal filter is represented by a transfer function $S(\Omega_X, \Omega_Y)$.

The quality of the restored image is represented by two parameters. The "restored bandwidth", $\Delta\tilde{\Omega}$, is defined by

$$\Delta\tilde{\Omega} = \left[\pi^{-1} \iint\limits_{-\infty}^{\infty} |\hat{B}\hat{H}| d\Omega_X d\Omega_Y \right]^{\frac{1}{2}} \tag{1}$$

where $\hat{B}$ and $\hat{H}$ are both normalized to have value unity at the origin. The mean-squared signal-to-noise ratio in the restored image is defined by [1, pp.16,17]

$$Q = \frac{(\overline{N})^2 \iint\limits_{-\infty}^{\infty} |\hat{S}|^2 \hat{\phi}_o \, d\Omega_X d\Omega_Y}{\varepsilon} - 1 \tag{2}$$

where $\overline{N}$ represents the mean number of photoevents detected in the image, $\hat{\phi}_o$ is the spectral density of the object, and ε is the expected value of the total mean-squared error in the restored image. We have previously

- 2 -

shown that ε is given explicitly by [1, p.16]

$$\varepsilon = \iint_{-\infty}^{\infty} \frac{(\overline{N})^2 |\hat{S}|^2 \hat{\phi}_o}{1 + \overline{N}|\hat{B}|^2 \hat{\phi}_o} \; d\Omega_X d\Omega_Y \tag{3}$$

The normalized spectral density of the object, $\hat{\phi}_o$, was shown [1, pp.18-21] to depend on the complexity of the object. In the case of an object representable as a windowed sample function of a stationary random process, the normalized spectral density was found to drop rapidly from unity to a level $(\sigma_o/\overline{o})^2 (A_c/A)$, where σ_o and $\overline{o}$ are, respectively, the standard deviation and mean of the object radiance distribution, A_c is the correlation area of the object, and A is the area of the total object field. In the results to be presented later, we shall always assume that the object is a point source $(\hat{\phi}_o = 1)$. However, to a good approximation the results can be applied to more complicated objects provided the parameter $\overline{N}$ is interpreted as being equal to $(\sigma_o/\overline{o})^2 \overline{n}$, where $\overline{n}$ represents the average number of photoevents arising from a single correlation area of the object.

III. RESTORATION OF ATMOSPHERICALLY DEGRADED IMAGES

In our previous report we showed plots of $\Delta\tilde{\Omega}$ and Q vs. $\overline{N}$ for values of r_o (the coherence length of the atmospheric distortions) of 5cm and 10cm, and for a flat ideal transfer function

$$\hat{S}(\Omega_X, \Omega_Y) = \begin{cases} 1 & \left(\Omega_X^2 + \Omega_Y^2\right)^{\frac{1}{2}} < \Omega_c \\ \\ 0 & \text{otherwise} \end{cases} \tag{4}$$

- 3 -

where Ω_0 is the diffraction-limited cutoff frequency of the telescope. We have extended the calculations to include in addition the cases of $r_0 = 20$cm and $r_0 = \infty$ (diffraction limited), and we have modified our choice of the ideal transfer function, using instead the diffraction-limited transfer function,

$$\hat{S}(\Omega) = \frac{2}{\pi} \left\{ \cos^{-1} \frac{\Omega}{\Omega_0} - \frac{\Omega}{\Omega_0} \sqrt{1 - \left(\frac{\Omega}{\Omega_0}\right)^2} \right\} \tag{5}$$

for $\Omega \leq \Omega_0$, where $\Omega = \left(\Omega_X^2 + \Omega_Y^2\right)^{\frac{1}{2}}$.

Our reason for changing the choice of $\hat{S}$ lies in a pathological behavior associated with the flat-topped $\hat{S}$. When $\overline{N}$ has reached such a large value that the restored bandwidth $\Delta\tilde{\Omega}$ has essentially achieved the value associated with a diffraction-limited transfer function, we intuitively expect the signal-to-noise ratio Q to increase in proportion to $\overline{N}$ for higher light levels, in accord with the Poisson character of the noise. Unfortunately, when a flat-topped $\hat{S}$ is used, Q ultimately increases as $\overline{N}^{1/3}$, a consequence of the fact that the restoration filter places too great an emphasis on restoring frequency components that are extremely close to the cutoff frequency Ω_0. To complicate matters even further, our previous plots of Q were found to ultimately increase as $\overline{N}^{\frac{1}{2}}$, rather than $\overline{N}^{1/3}$. This behavior was found to arise from our use of an approximate expression for the diffraction limited OTF [1, Eq. (59)] which approaches zero at a different rate than the exact expression. To remove this pathological dependence of Q on the behavior of the OTF infinitesimally close to cutoff, we have found it highly desirable to use the $\hat{S}$ of Eq. (5). This choice has the added advantage that the ideally filtered object will always be non-negative, whereas this is not

- 4 -

necessarily the case with a flat-topped $\hat{S}$.

The blur transfer function assumed here (as in the previous report) is of the form

$$\hat{B}(\Omega) = \hat{B}_T(\Omega)\hat{B}_A(\Omega) \tag{6}$$

where $\hat{B}_T(\Omega)$ is the optical transfer function of the telescope, while $\hat{B}_A(\Omega)$ is the optical transfer function of the atmosphere. For simplicity, we assume that the telescope has a clear circular aperture (no central obscuration) and is diffraction limited, in which case

$$\hat{B}_T(\Omega) = \frac{2}{\pi}\left\{\cos^{-1}\frac{\Omega}{\Omega_0} - \frac{\Omega}{\Omega_0}\left[1 - \left(\frac{\Omega}{\Omega_0}\right)^2\right]^{\frac{1}{2}}\right\} \tag{7}$$

for $\Omega \leq \Omega_0$. For the atmospheric OTF, we assume that the exposure time is long compared to the atmospheric fluctuation time, and use an OTF of the form

$$\hat{B}_A(\Omega) = \exp\left\{-3.44\left(\frac{\Omega}{\Omega_0}\right)^{5/3}\left(\frac{D}{r_o}\right)^{5/3}\left[1 - \alpha\left(\frac{\Omega}{\Omega_0}\right)^{1/3}\right]\right\} \tag{8}$$

for $\Omega \leq \Omega_0$. Here D is the diameter of the telescope aperture and α takes on the values 0, ½ or 1 as follows:

$\alpha = 0$: No tilt removal;

$\alpha = ½$: Perfect tilt removal, far field atmospheric
propagation;

$\alpha = 1$: Perfect tilt removal, near field atmospheric
propagation.

Tilt removal refers to the case of a telescope with a servo-controlled mirror which removes the linear terms in a least-squares fit to the atmospherically distorted wavefront. The result is nearly (but not

- 5 -

exactly) the same as using a perfect centroid tracker to determine the required mirror tilt.

In Fig. 2a, b and c, we present the plots of restored bandwidth $\Delta\tilde{\Omega}$ vs. $\overline{N}$ for the three cases described above. The curve for $r_o = \infty$ represents the ideal behavior of a diffraction-limited telescope in the absence of atmospheric turbulence. In all cases the telescope mirror diameter was assumed to be 1.524 meters (60 inches) and the mean wavelength was taken to be 5×10^{-7} meters. For large enough $\overline{N}$, all of the curves eventually reach the diffraction-limited performance curve $(r_o = \infty)$, but for the range of $\overline{N}$ shown, only the $r_o = 20$cm curve of Fig. 2(c) accomplishes this.

Also shown on each drawing are three dotted horizontal lines. These lines represent the value of $\Delta\tilde{\Omega}$ for $r_o = 5$cm, 10cm and 20cm when no post processing is applied to the detected image (i.e., $\hat{H} = 1$ for $\Omega \leq \Omega_0$, zero otherwise). By comparing the corresponding dotted and solid lines, it is possible to deduce quantitatively just how much image bandwidth has been gained by using the least-squares restoration filter.

Figures 3a, b and c present plots of the signal-to-noise ratio Q vs. $\overline{\overline{N}}$, again for four values of r_o. eventually, all of these curves bend upwards and increase in proportion to $\overline{N}$, running parallel to, but below, the $r_o = \infty$ curve. However, for the range of $\overline{N}$ shown, this upward turn can be seen only for the $r_o = 20$cm curve of Fig. 3(c). By comparing Figs. 2(c) and 3(c), we note that the upward turn in Q takes place at values of $\overline{N}$ where the restored bandwidth is closely approaching the diffraction-limited curve $(r_o = \infty)$. Thus, once the restoration filter has succeeded in restoring frequency components to the level appropriate

- 6 -

Fig. 2. $\Delta\tilde{\Omega}$ vs. $\overline{N}$ for (a) long exposure, no tilt, removal, (b) long exposure, tilt removal, far field atmospheric propagation, and (c) long exposure, tilt removal, near field atmospheric progagation.

- 7 -
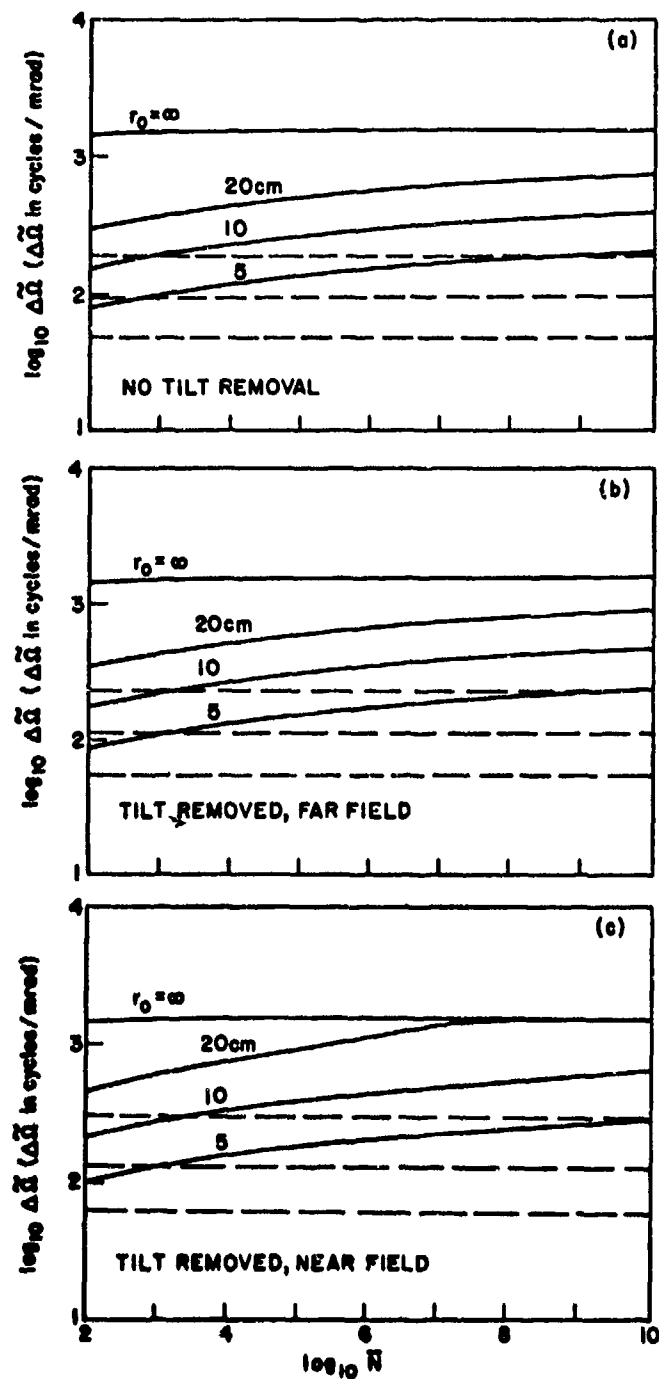
Fig. 3. Q vs. $\overline{N}$ for (a) long exposure, no tilt,
removal, (b) long exposure, tilt removal, far
field atmospheric propagation, and (c) long
exposure, tilt removal, near field atmospheric
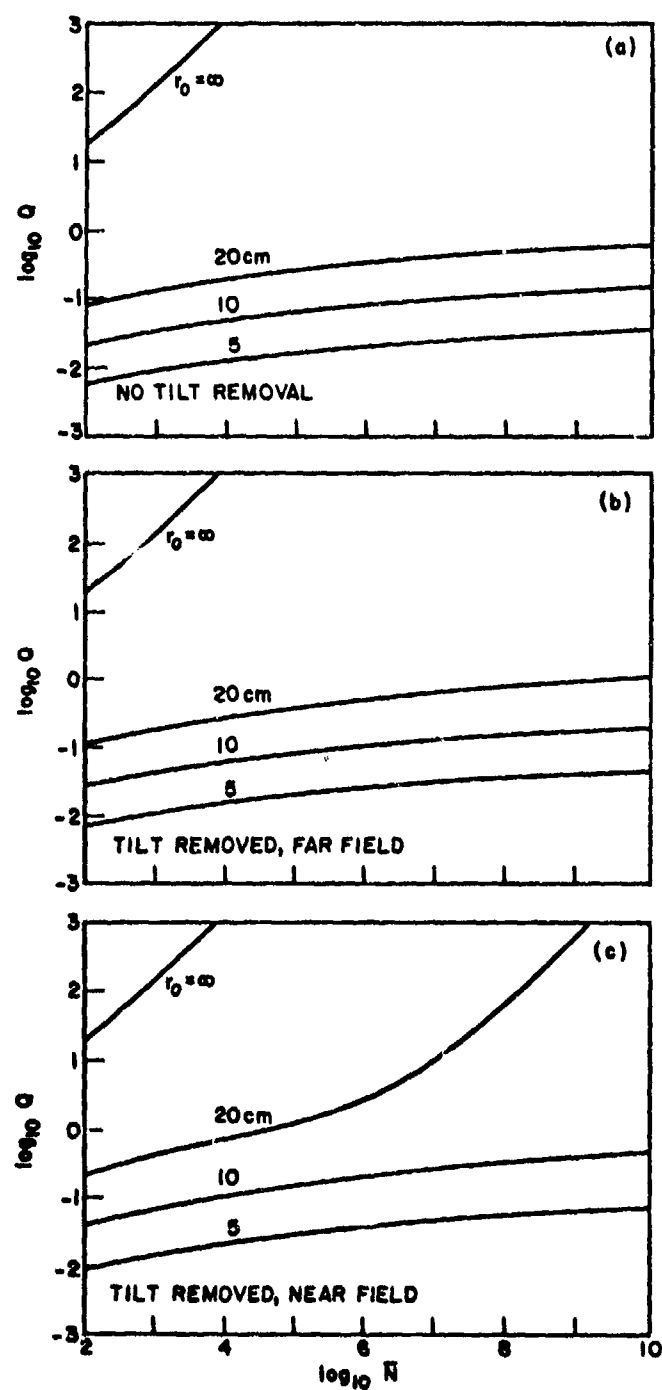propagation.

- 8 -

for a diffraction-limited telescope, all further increases of $\overline{N}$ have the effect only of increasing the signal-to-photon-noise ratio, with a resulting increase of Q in proportion to $\overline{N}$. For the $r_0 = 10$cm, perfect tilt removed, near field curve, this transition has been found to take place at $\overline{N} = 10^{21}$, which is far off the scale of $\overline{N}$ shown.

IV. PERFORMANCE OF A SYSTEM WITH BOTH PREDETECTION COMPENSATION AND POSTDETECTION COMPENSATION

We consider now the photon-limited performance of a system which utilizes both predetection compensation and postdetection compensation. With reference to Fig. 4, a portion of the incoming light is sent to a wavefront sensing system, which measures the atmospheric wavefront distortions in real time. The wavefront sensor then drives a wavefront corrector (usually a deformable mirror), which removes the atmospheric distortions from the incoming light. In addition, a portion of the light
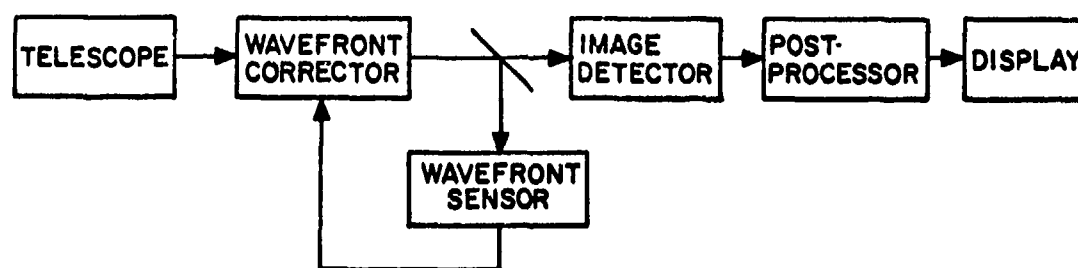

Fig. 4. Compensated imaging system block diagram

- 9 -

leaving the wavefront corrector is sent directly to an image detector. The detected image is then subjected to post-processing, following which the final image is displayed.

Two types of error arise in this system as a result of the finite photon flux available at the telescope. First, the wavefront sensor functions imperfectly in the presence of photon noise, with the result that to some extent the wavefront is improperly corrected, and the recorded image suffers residual blur. Secondly, the finite photon flux sent to the image detector limits the ability of the post-processor to remove these residual defects.

Our goal is to study image quality, as fined by the two parameters $\Delta\tilde{\Omega}$ and Q of the previous section, as a function of the mean number of photoevents $\overline{N}$ supplied by telescope. The post-processor will again be a linear invariant least squares filter. In fact, the entire formalism represented by Fig. 1 can again be used, but with a blur transfer function appropriate for the partially precompensated system.

Our model for the partially compensated wavefronts is that of a spatially stationary gaussian random phase screen. This model is, of course, only an approximation, for the fixed locations of the discrete actuators on the deformable mirror introduce a spatial non-stationarity, sometimes referred to as the "waffle effect". However, the statistically stationary phase screen provides a reasonable first order model. From such a model, it is easily shown that the blur transfer function associated with the partially compensated wavefronts is of the form

$$\hat{B}_c(\Omega) = \exp\left\{-\frac{1}{2} D_\phi(\overline{\lambda}\Omega)\right\} \tag{9}$$

where $\overline{\lambda}$ is the mean wavelength and $D_\phi(r)$ is the structure function of

-10 -

the residual phase errors,

$$D_\phi(r) = E\left[(\phi_1 - \phi_2)^2\right] \qquad (10)$$

Here ϕ_1 and ϕ_2 are two values of the phase at points separated by distance r, and it has been tacitly assumed that the structure function is circularly symmetric. Implicit in this model is the assumption of "near field" atmospheric propagation, i.e., intensity scintillation effects are negligible.

In evaluating the performance of the overall system, we have found it necessary to specify the character of the precompensation system more precisely. We assume here that the wavefront sensor consists of a shearing interferometer that produces an array of noisy phase-difference measurements. These measurements are applied to a phase reconstruction network, which produces an array of noisy phase estimates from the phase difference measurements. The phase estimates are then used to drive a deformable mirror. In general, the phase estimates are based on a measurement interval that is some small fraction of the total integration time used to detect the corrected image. In the specific results presented later we have assumed a ratio of total image integration time T to phase measurement time τ of 10^4. This ratio is appropriate, for example, when $T = 1$ second and $\tau = 100$ microseconds. We shall further assume that any errors induced by the fact that the active mirror is driven to correct for errors that were measured a short time in the past are negligible. In other words, we assume that the delay between measurement and correction is negligibly small compared to the other errors.

The phase structure function consists of two parts,

$$D_\phi(r) = D_\phi^{(f)}(r) + D_\phi^{(n)}(r) \quad , \tag{11}$$

where $D_\phi^{(f)}(r)$ is the structure function component due to fitting error and $D_\phi^{(n)}(r)$ is the structure function component due to noise. McGlamery [2] has estimated these structure functions by simulation of a system having 317 subapertures within a 1.6 meter aperture. In turn, we have fit McGlamery's simulation results with analytic expressions. We find excellent fit to the simulation data by the following expressions:

$$D_\phi^{(f)}(\overline{\lambda\Omega}) = 2\sigma_f^2\left[1 - e^{-\left(54.4\frac{\Omega}{\Omega_0}\right)^2}\right]$$

$$D_\phi^{(n)}(\overline{\lambda\Omega}) = 2\sigma_n^2\left[1 - e^{-\left(4.76\frac{\Omega}{\Omega_0}\right)^{1.22}}\right] \quad . \tag{12}$$

Here σ_f^2 and σ_n^2 are the phase variances due to fitting error and noise, respectively.

Using Hudgin's [3] results, we can express σ_f^2 as

$$\sigma_f^2 = 0.316\left(\frac{L_a}{r_o}\right)^{5/3} \quad (rad)^2 \tag{13}$$

where L_a is the spacing of the actuators. With K subapertures in an unobstructed aperture of diameter D meters, we have approximately that

$$\sigma_f^2 = 0.316\left(\frac{D}{\sqrt{K}\,r_o}\right)^{5/3} \quad . \tag{14}$$

Turning attention to the phase variance due to noise, it is well established that the variance of the electronic phases measured by the

wavefront sensor are

$$\sigma_\varepsilon^2 = \frac{2}{\gamma^2 \overline{N}_s} \quad (\text{rad})^2 \tag{15}$$

where γ is the electronic fringe contrast and $\overline{N}_s$ is the average number of photoevents per phase-difference sensor. For a point-source object, we assume $\gamma^2 = 1$. Taking account of the fact that there are two shears involved, one with respect to x and the second with respect to y, we have

$$\overline{N}_s = \frac{\beta \overline{N} \tau}{2KT} \tag{16}$$

where β is the fraction of photoevents sent to the wavefront sensor $(0 < \beta < 1)$, and $\overline{N}$ is the total number of photoevents collected by the telescope. (Implicit in our expressions are the assumptions of equal losses and equal quantum efficiencies in the wavefront sensing and image detecting branches of the optical system.) Thus, for a point source object,

$$\sigma_\varepsilon^2 = \frac{4KT}{\beta \overline{N} \tau} \quad (\text{rad})^2 \quad . \tag{17}$$

The variance of the phase difference measurements is related to σ_ε^2 through

$$\sigma_{\Delta\phi}^2 = \left(\frac{L_s}{S}\right)^2 \sigma_\varepsilon^2 \tag{18}$$

where S is the shear distance and L_s is the sensor spacing. For a point source object, we assume that the shear distance can be made as big as the sensor spacing, yielding $\sigma_{\Delta\phi}^2 = \sigma_\varepsilon^2$.

We use Fried's results [4] to relate the variance of the estimated phases to the variances of the phase differences,

$$\sigma_n^2 = 0.6558[1 + 0.2444 \ln K] \sigma_{\Delta\phi}^2 . \tag{19}$$

- 13 -

Combining (19), (18), and (17), we find

$$\sigma_n^2 = 0.6558[1 + 0.2444 \ln K]\left(\frac{4KT}{\beta \bar{N}\tau}\right) \qquad (20)$$

Equations (9), (12), (14) and (20) now provide us with a complete specification of the optical transfer function of the precompensation system. This transfer function must be multiplied by the telescope transfer function $\hat{B}_T(\Omega)$ to obtain the entire blur transfer function.

Finally, we take into account the effect of the post-compensation system. Noting that the average number of photoevents appearing in the image is $(1-\beta)\bar{N}$, and using $\hat{S} = \hat{B}_T$ for the ideal filter, we use Eq. (47) of Ref. 1 to write the product of blur and deblur OTF's as

$$\hat{B}\hat{H} = \frac{[1 + (1-\beta)\bar{N}]\hat{B}_T^3 \hat{B}_c^2}{1 + (1-\beta)\bar{N} \hat{B}_T^2 \hat{B}_c^2} \qquad , \qquad (21)$$

where a point-source object $(\hat{\phi}_o = 1)$ has been explicitly assumed. From this quantity, the image quality parameters $\Delta\tilde{\Omega}$ and Q can be calculated by numerical integration,

$$\Delta\tilde{\Omega} = \left[2 \int\limits_0^\infty \Omega |\hat{B}(\Omega)\hat{H}(\Omega)| d\Omega\right]^{\frac{1}{2}} \qquad (22)$$

and

$$Q = (1-\beta)\bar{N} \frac{\displaystyle\int\limits_0^\infty \frac{\hat{B}_T^4(\Omega)\hat{B}_c^2(\Omega) \, \Omega \, d\Omega}{1 + (1-\beta)\bar{N} \, \hat{B}_T^2(\Omega)\hat{B}_c^2(\Omega)}}{\displaystyle\int\limits_0^\infty \frac{\hat{B}_T^2(\Omega) \, \Omega \, d\Omega}{1 + (1-\beta)\bar{N} \, \hat{B}_T^2(\Omega)\hat{B}_c^2(\Omega)}} \qquad . \qquad (23)$$

We now present results of computer calculations of $\Delta\tilde{\Omega}$ and Q based on the theory outlined above. In all cases a single point-source object is assumed, and the number of wavefront-sensor subapertures is

317. Figures 5a and b show plots of $\Delta\widetilde{\Omega}$ and Q vs. $\overline{N}$ for $r_o = 10cm$ and three different values of β (0.3, 0.9, 0.99). Note that the diffraction limited bandwidth is reached for $\overline{N}$ in the range 10^6 to 10^7, depending on β. The values of Q achieved are highest for large β when $\overline{N}$ is below the value which achieves diffraction limited perform-ance. However, for values of $\overline{N}$ above this level, small values of β are superior. Once diffraction limited bandwidth has been reached, there is no point to sending more light to the wavefront sensor. Hence smaller and smaller fractions of the incident light should be sent to the wavefront sensor as $\overline{N}$ increases beyond its critical value.

The optimization of the splitting ratio β is explored in more detail in Figs. 6a and b. $\Delta\widetilde{\Omega}$ and Q are shown as functions of β for various values of $\overline{N}$, with r_o fixed at 10cm. The optimum value of β is best determined from Q in Fig. 6b, for $\Delta\widetilde{\Omega}$ ultimately saturates at the diffraction-limited bandwidth, while Q has no such saturation limit. The optimum value of β is seen to depend rather strongly on the object brightness $\overline{N}$. For $\overline{N}$ small $(<10^7)$, the optimum β is close to unity, indicating that most of the light should be sent to the wavefront sensor. However, for $\overline{N}$ greater than about 10^7, the optimum value of β shifts abruptly to rather small values, indicating that most of the light should be sent to the image detector. This behavior simply indicates once again that when $\Delta\widetilde{\Omega}$ has reached the diffraction limit, further increases of light flux should be allocated to the image detector for best performance.

Figures 7a and b show the dependence of system performance on the atmospheric coherence diameter r_o. In this case β is fixed at 0.9; $\Delta\widetilde{\Omega}$ and Q are plotted vs. $\overline{N}$. Concentrating on Fig. 7b, for $\overline{N}$
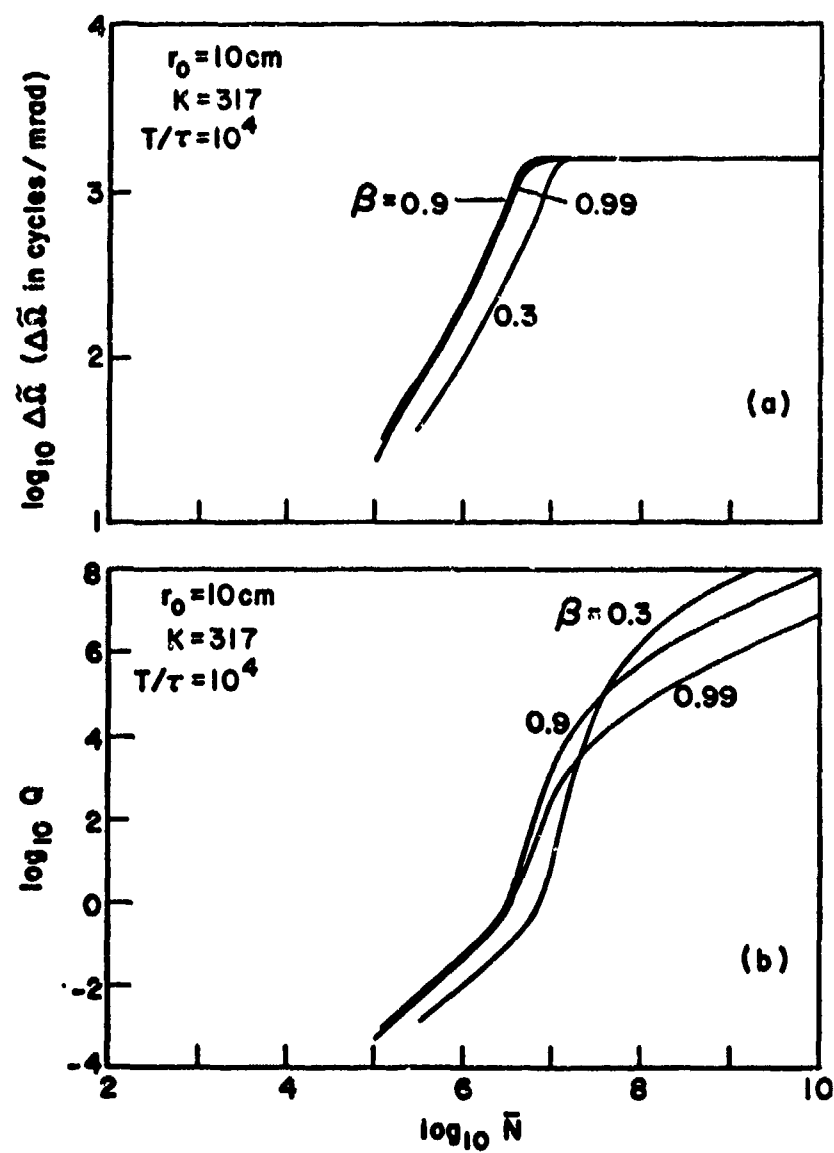
Fig. 5. Restored bandwidth (a) and quality
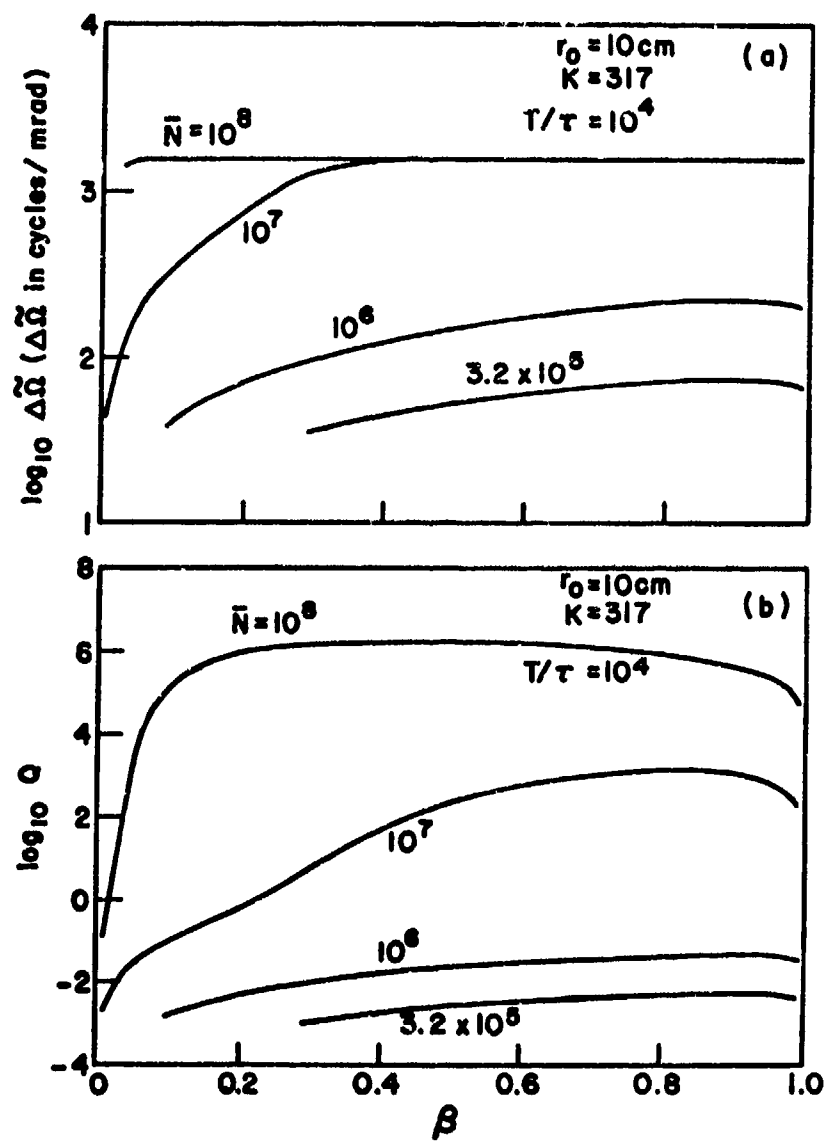factor (b) vs. $\bar{N}$ for $r_0 = 10$cm and
three values of β.

- 16 -

Fig. 6. Restored bandwidth (a) and quality factor (b) vs. β for r_0=10cm and various values of $\bar{N}$.
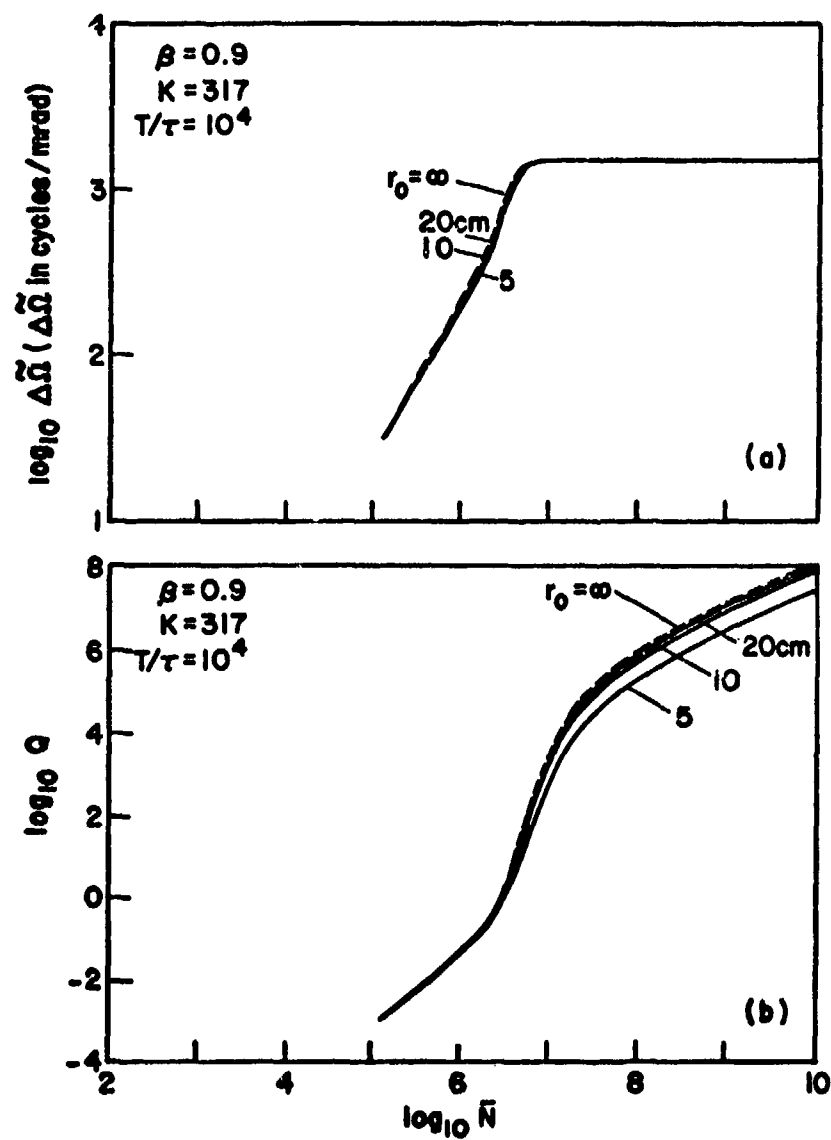
Fig. 7. Restored bandwidth (a) and quality factor
(b) vs. $\overline{N}$ for $\beta = 0.9$ and four values of
r_0.

below the critical range of values that produce diffraction-limited bandwidth, the difference of values of Q achieved as r_o varies is small. For $\bar{N}$ above this critical range, the change in Q as r_o varies is larger, but less than an order of magnitude.

In the final figure (Fig. 8), we investigate the effects of removing certain parts of the overall pre- and post-compensated imaging system. Plots of $\Delta\tilde{\Omega}$ vs. $\bar{N}$ are shown, with r_o fixed at 10cm. Curves are shown for pre- and post-compensation ($\beta = 0.9$), pre-compensation alone ($\beta = 0.9$), post-compensation alone ($\beta = 1.0$, with and without simple tilt removal). A number of observations can be made from these curves. First, comparing the curve for pre-compensation only (b) with the curve for both pre- and post-compensation (a), we see the differences are greatest in the transition region where the restored bandwidth
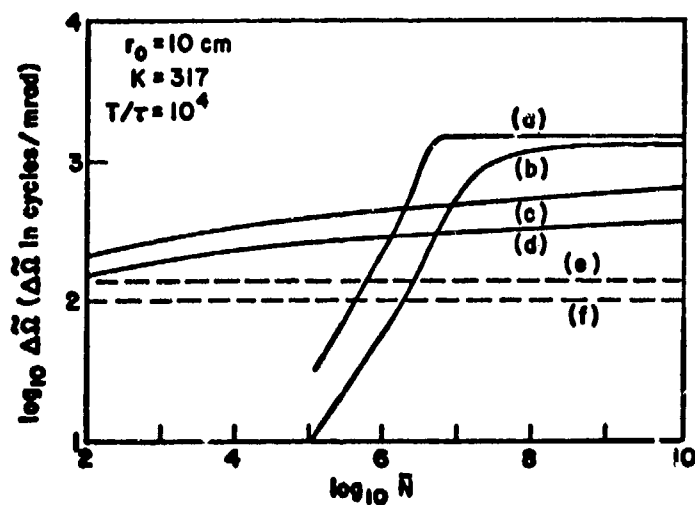

Fig. 8. Comparison of $\Delta\tilde{\Omega}$ vs. $\bar{N}$ curves for various compensation systems.
(a) Precompensation and Postcompensation.
(b) Precompensation Only.
(c) Postcompensation and Tilt Removal, Near Field.
(d) Postcompensation, Long Exposure.
(e) Tilt Removal Only, Near Field.
(f) No Compensation, Long Exposure.

- 19 -

is approaching saturation. For larger values of $\overline{N}$, the difference

between the two saturation levels is attributable to fitting errors. In

one case the effects of fitting errors are post-compensated, in the

second case they are not.

Next we note that over a large range of $\overline{N}$, the values of $\Delta\widetilde{\Omega}$

achieved with post-compensation only fall far below those achieved with

pre-compensation only. This conclusion remains valid whether overall

tilt removal is used or not in the post-compensation case. Note, however,

that if $\overline{N}$ is sufficiently small, ultimately the pre-compensation

system begins to degrade the performance, for the wavefront measurements

become so noisy that they add errors that are worse than those intro-

duced by the atmosphere. Thus, for example, with $\overline{N} = 10^4$, best per-

formance is achieved by turning the pre-compensation system off and

performing only post-compensation. However, the values of $\Delta\widetilde{\Omega}$ achieved

in this regime are not much better than what could be achieved with the

unmodified original telescope without any post-compensating.

V.   SENSITIVITY OF SPECKLE IMAGING

By the term "speckle imaging" we mean the technique introduced by

Labeyrie [5] which depends on averaging the spectral density distributions

of a sequence of κ short-exposure photographs. If $\hat{I}_j(\nu)$ represents

the Fourier transform of the jth short-exposure image $i_j(x)$, normal-

ized to have value unity at the origin, then

$$\hat{I}_j(\nu) = \hat{B}_j(\nu)\hat{O}(\nu)$$

where $\hat{B}_j(\nu)$ represents the optical transfer function (OTF) of the kth

exposure, and $\hat{O}(\nu)$ represents the normalized Fourier spectrum of the

object (assumed identical for all κ measurements).

- 20 -

The Labeyrie technique uses κ independent measurements of $|\hat{I}_j(\nu)|^2$ to attempt to estimate $|\hat{O}(\nu)|^2$. The basis for this method rests upon the relation

$$\left\langle |\hat{I}_j(\nu)|^2 \right\rangle = \left\langle |\hat{B}_j(\nu)|^2 \right\rangle |\hat{O}(\nu)|^2 \qquad (24)$$

and the fact that [6], in the mid-frequency region of the diffraction-limited OTF,

$$\left\langle |\hat{B}_j(\nu)|^2 \right\rangle \cong \left(\frac{r_o}{D}\right)^2 B_T(\nu) \qquad (25)$$

where r_o is Fried's atmospheric coherence diameter; D is the diameter of the telescope used; $\hat{B}_T(\nu)$ represents the diffraction-limited OTF of the telescope; and it has been assumed that $D/r_o \gg 1$. Thus in the mid-frequency range of the telescope passband,

$$\left\langle |\hat{I}_j(\nu)|^2 \right\rangle \cong \frac{r_o}{D}^2 \hat{B}_T(\nu) |\hat{O}(\nu)|^2 \qquad (26)$$

where D, r_o and $\hat{B}_T$ are presumed known, $|\hat{I}(\nu)|^2$ is to be estimated from the sequence of κ pictures, and $\left\langle |\hat{O}(\nu)|^2 \right\rangle$ is the ultimate quantity of interest.

For any particular sequence of κ pictures, the finite average $\frac{1}{\kappa} \sum_{j=1}^{\kappa} |I_j(\nu)|^2$ is only approximately equal to the true average $\left\langle |I_j(\nu)|^2 \right\rangle$. The statistical fluctuations of the finite average arise from two sources:

(1) The statistical fluctuations of $\hat{B}_j(\nu)$ from picture to picture, as caused by the changing atmospheric turbulence,

and

(2) The statistical fluctuations of $i_j(x)$ caused by the finite number of photoevents detected in each picture.

- 21 -

Both of these sources of fluctuations lead to errors in our estimate of $\left\langle |\hat{I}_j(\nu)|^2 \right\rangle$.

The effects of these two types of fluctuations on an estimate of $\left\langle |\hat{I}(\nu)|^2 \right\rangle$ have been evaluated in our previous technical report [1]. From Eq. (31) of that report, we have that the r.m.s signal-to-noise ratio associated with the measurement is, for a single frame $(\kappa = 1)$,

$$
\left(\frac{S}{N}\right)^{(1)} = \frac{\hat{\phi}_i(\nu)}{\left\{\hat{\phi}_i^2(\nu) + \frac{2}{\overline{N}}\hat{\phi}_i(\nu) + \frac{1}{(\overline{N})^2}\left[1 + 4\hat{\phi}_i(\nu) + \hat{\phi}_i(2\nu)\right] + \frac{1}{(\overline{N})^3}\right\}^{\frac{1}{2}}} \quad (27)
$$

where $\overline{N}$ is the average total number of photoevents detected in a single frame, and

$$
\hat{\phi}_i(\nu) \stackrel{\Delta}{=} \left\langle |\hat{I}(\nu)|^2 \right\rangle \quad . \tag{28}
$$

A similar expression has been derived by Roddier [7]. When the measurement is based on κ independent frames of data, the S/N is increased by $\sqrt{\kappa}$,

$$
\left(\frac{S}{N}\right)^{(\kappa)} = \sqrt{\kappa}\left(\frac{S}{N}\right)^{(1)} \quad . \tag{29}
$$

The frequency range of greatest interest is at the high end of the diffraction-limited telescope passband. Hence, if ν_0 represents the diffraction-limited cutoff frequency of the telescope, we assume that $\nu > \nu_0/2$, in which case the term $\hat{\phi}_i(2\nu)$ of Eq. (27) can be replaced by zero. For simplicity of notation we define

$$
\hat{\phi}_0(\nu) = |\hat{0}(\nu)|^2 \tag{30}
$$

to represent the normalized spectral density of the object itself, in which case Eq. (26) becomes

- 22 -

$$\hat{\phi}_i(\nu) = \left(\frac{r_o}{D}\right)^2 \hat{B}_T(\nu)\hat{\phi}_o(\nu). \tag{31}$$

Finally, we define the quantity

$$\overline{n} = \left(\frac{r_o}{D}\right)^2 \overline{N} \quad , \tag{32}$$

which represents the average number of photoevents per atmospheric coherence area. This number can equivalently be regarded as the average number of photoevents per speckle in the image.

With the above definitions and some simple algebraic manipulations, we obtain from Eq.(27),

$$\left(\frac{S}{N}\right)^{(1)} = \frac{\overline{n}\,\hat{B}_T(\nu)\hat{\phi}_o(\nu)}{\left\{\left[1 + \overline{n}\,\hat{B}_T(\nu)\hat{\phi}_o(\nu)\right]^2 + \frac{1}{\overline{N}}\left[1 + 4\overline{n}\,\hat{B}_T(\nu)\hat{\phi}_o(\nu)\right]\right\}^{\frac{1}{2}}} \tag{33}$$

valid for $\nu > \nu_o/2$.

Three important regions of this relationship can be identified, in each of which a different dependence on $\overline{n}$ is found

    (1) For $\overline{n}\,\hat{B}_T\hat{\phi}_o \gg 1$,

$$\left(\frac{S}{N}\right)^{(1)} \cong 1 \qquad (\text{independent of } \overline{n}) \quad ;$$

    (2) $\overline{n}\,\hat{B}_T\hat{\phi}_o \ll 1$ but $\overline{N} \gg 1$,

$$\left(\frac{S}{N}\right)^{(1)} \cong \overline{n}\,\hat{B}_T(\nu)\hat{\phi}_o(\nu) \quad ;$$

    (3) $\overline{n}\,\hat{B}_T\hat{\phi}_o \ll 1$ but $\overline{N} \ll 1$,

$$\left(\frac{S}{N}\right)^{(1)} = (\overline{n})^{3/2}\left(\frac{D}{r_o}\right)\hat{B}_T(\nu)\hat{\phi}_o(\nu) \quad .$$

Two important points should be emphasized. First, the maximum possible

- 23 -

single-frame signal-to-noise ratio for speckle interferometry is unity, regardless of how bright the object may be. Second, only when the average number of photoevents per <u>picture</u> is much less than unity does increasing the telescope aperture diameter improve the signal-to-noise ratio.

The single-frame signal-to-noise ratio is plotted in Fig. 9 for the special case $D = 1.52$ meters, $r_o = 10$cm, $\nu/\nu_o = 0.8$ and $\hat{\phi}_o = 1$.
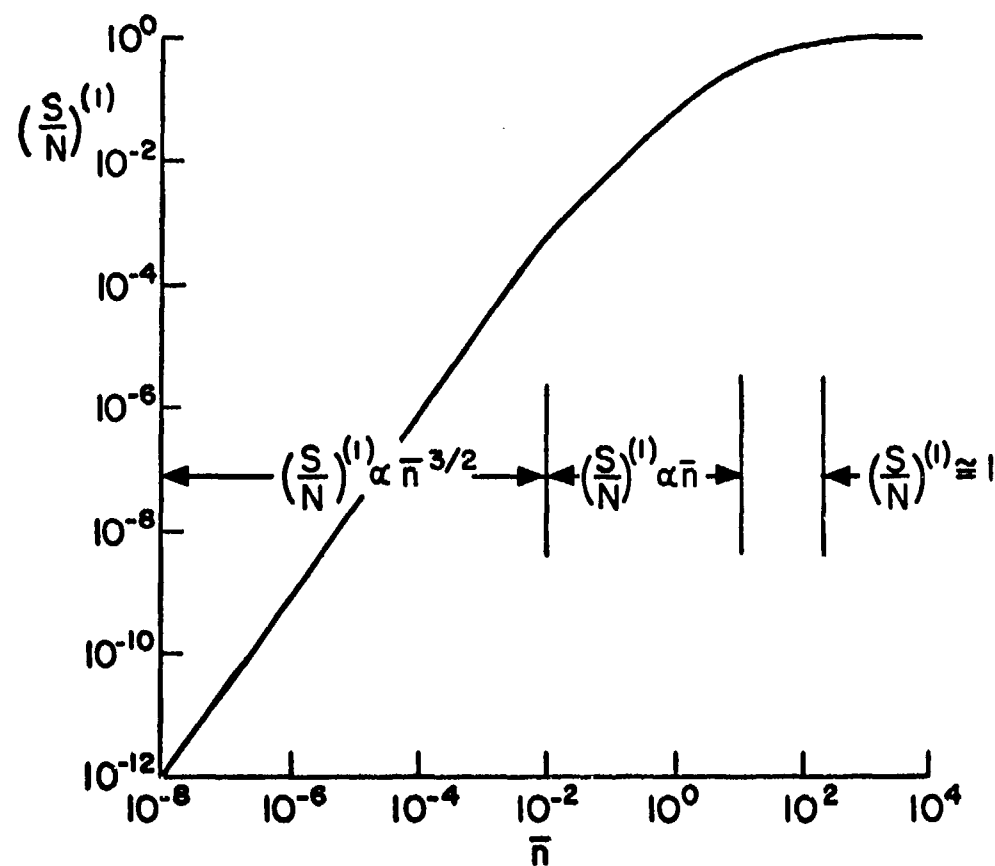

Fig. 9. Single-frame rms signal-to-noise ratio vs. average number of photoevents per r_o-cell, speckle imaging.

The three separate regions of dependence on $\bar{n}$ are clearly distinguishable.

REFERENCES

[1]   J.W.Goodman and J.F. Belsher, "Photon Limited Images and Their
        Restoration", Tech. Report RADC-TR-76-50, Defense Advanced Research
        Projects Agency, March 1976, (A024027).

[2]   Private communication, B.J. McGlamery, Scripps Institution of
        Oceanography, University of California, San Diego, California.

[3]   R.H. Hudgin, "Wavefront Compensation Error due to Finite Corrector
        Element Size", Meeting of the Optical Society of America,
        October 1975.

[4]   D.L. Fried, "Predetection Compensated Imaging Theory", Tech.
        Report RADC-TR-76-103, Defense Advanced Research Projects Agency,
        April 1976, (A024393).

[5]   A. Labeyrie, Astron. & Astrophys. 6, 85 (1970).

[6]   D. Korff, "Analysis of a Method for Obtaining Near-Diffraction-
        Limited Information in the Presence of Atmospheric Turbulence",
        J. Opt. Soc. Am., 63, 971, August 1973.

[7]   F. Roddier, "Signal-to-Noise Ratio in Speckle Interferometry
        Imaging in Astronomy", (Technical Digest), Topical Meeting of
        Optical Society of America, June 1975

METRIC SYSTEM

BASE UNITS:

Quantity	Unit	SI Symbol	Formula
length	metre	m	...
mass	kilogram	kg	...
time	second	s	...
electric current	ampere	A	...
thermodynamic temperature	kelvin	K	...
amount of substance	mole	mol	...
luminous intensity	candela	cd	...

SUPPLEMENTARY UNITS:

Quantity	Unit	SI Symbol	Formula
plane angle	radian	rad	...
solid angle	steradian	sr	...

DERIVED UNITS:

Quantity	Unit	SI Symbol	Formula
Acceleration	metre per second squared	...	m/s
activity (of a radioactive source)	disintegration per second	...	(disintegration)/s
angular acceleration	radian per second squared	...	rad/s
angular velocity	radian per second	...	rad/s
area	square metre	...	m
density	kilogram per cubic metre	...	kg/m
electric capacitance	farad	F	A·s/V
electrical conductance	siemens	S	A/V
electric field strength	volt per metre	...	V/m
electric inductance	henry	H	V·s/A
electric potential difference	volt	V	W/A
electric resistance	ohm		V/A
electromotive force	volt	V	W/A
energy	joule	J	N·m
entropy	joule per kelvin	...	J/K
force	newton	N	kg·m/s
frequency	hertz	Hz	(cycle)/s
illuminance	lux	lx	lm/m
luminance	candela per square metre	...	cd/m
luminous flux	lumen	lm	cd·sr
magnetic field strength	ampere per metre	...	A/m
magnetic flux	weber	Wb	V·s
magnetic flux density	tesla	T	Wb/m
magnetomotive force	ampere	A	...
power	watt	W	J/s
pressure	pascal	Pa	N/m
quantity of electricity	coulomb	C	A·s
quantity of heat	joule	J	N·m
radiant intensity	watt per steradian	...	W/sr
specific heat	joule per kilogram-kelvin	...	J/kg·K
stress	pascal	Pa	N/m
thermal conductivity	watt per metre-kelvin	...	W/m·K
velocity	metre per second	...	m/s
viscosity, dynamic	pascal-second	...	Pa·s
viscosity, kinematic	square metre per second	...	m/s
voltage	volt	V	W/A
volume	cubic metre	...	m
wave number	reciprocal metre	...	(wave)/m
work	joule	J	N·m

SI PREFIXES:

Multiplication Factors	Prefix	SI Symbol
$1\ 000\ 000\ 000\ 000 = 10^{12}$	tera	T
$1\ 000\ 000\ 000 = 10^{9}$	giga	G
$1\ 000\ 000 = 10^{6}$	mega	M
$1\ 000 = 10^{3}$	kilo	k
$100 = 10^{2}$	hecto*	h
$10 = 10^{1}$	deka*	da
$0.1 = 10^{-1}$	deci*	d
$0.01 = 10^{-2}$	centi*	c
$0.001 = 10^{-3}$	milli	m
$0.000\ 001 = 10^{-6}$	micro	μ
$0.000\ 000\ 001 = 10^{-9}$	nano	n
$0.000\ 000\ 000\ 001 = 10^{-12}$	pico	p
$0.000\ 000\ 000\ 000\ 001 = 10^{-15}$	femto	f
$0.000\ 000\ 000\ 000\ 000\ 001 = 10^{-18}$	atto	a

* To be avoided where possible.